Ray tracing and ECRH absorption modeling in the HSX stellarator

Ray tracing and ECRH absorption modeling in the HSX stellarator

G.M. Weir[1], K.M. Likin[1], N.B. Marushchenko[2] and Y. Turkin[2]

[1] HSX Plasma Laboratory, University of Wisconsin–Madison, Madison, WI 53706, USA
[2] Max Planck Institute for Plasma Physics, EURATOM Association, Wendelsteinstr. 1, 17491 Greifswald, Germany

E-mail: weir@wisc.edu

CrossMark

Abstract

To increase flexibility in ECRH experiments on the helically symmetric experiment (HSX), a second gyrotron and transmission line have been installed. The second antenna includes a steerable mirror for off-axis heating, and the launched power may be modulated for use in heat pulse propagation experiments. The extraordinary wave at the second harmonic of the electron gyrofrequency or the ordinary wave at the fundamental resonance are used for plasma start-up and heating on HSX. The tracing visualized ray tracing code (Marushchenko *et al* 2007 *Plasma Fusion Res.* **2** S1129) is used to estimate single-pass absorption and to model multi-pass wave damping in the three-dimensional HSX geometry. The single-pass absorption of the ordinary wave at the fundamental resonance is calculated to be as high as 30%, while measurements of the total absorption indicate that 45% of the launched power is absorbed. A multi-pass ray tracing model correctly predicts the experimental absorption and indicates that the launched power is absorbed within the plasma core ($r/a \leqslant 0.2$).

(Some figures may appear in colour only in the online journal)

1. Introduction

Electron cyclotron resonant heating (ECRH) has become a fundamental component of heating schemes in fusion experiments [1], and modeling is necessary in the design of new systems, as well as in the characterization of implemented systems, in experiments with 3D magnetic fields.

The helically symmetric experiment (HSX) is a four field period stellarator device in which the magnetic field strength is helically symmetric [2–4]. For the work presented in this paper the propagation and absorption of electron cyclotron waves is modeled using the tracing visualized (TRAVIS) ray tracing code [5, 6]. At low plasma density, $n_e \leqslant 10^{19}$ m^{-3}, the absorption of electron cyclotron waves is less than 50% for the electron temperatures achieved in HSX, $T_e \leqslant 2.5$ keV. The TRAVIS code calculates the absorption of electron cyclotron waves in plasma, and the code is capable of modeling multiple passes through the plasma upon reflection from the stainless steel vessel wall of HSX.

The HSX vacuum vessel, magnetic field, and ECRH antennas are described in section 2. This section also describes the discretization of the wave launched from each antenna used in ray tracing calculations. Single-pass ray tracing results are presented in section 3, and multi-pass absorption calculations are compared to an absorption measurement in section 4.

2. Ray tracing calculations using the TRAVIS code

Two ECRH antennas are used for plasma start-up and heating in HSX. Each transmission line is connected to a 28 GHz Varian gyrotron (VGA-8050M), which has been rated for 200 kW of output power over a 75 ms pulse length. Both antennas are comprised of an open-ended cylindrical waveguide and a focusing ellipsoidal mirror within the vacuum chamber. 48 modular coils are used to produce the main, quasi-helically symmetric, magnetic configuration of HSX [7], and in this work, the magnetic equilibria used with the TRAVIS code are calculated using the VMEC code [8].

The vacuum vessel of HSX is shaped to match the contours of the Last Closed magnetic Flux Surface (LCFS) in the quasi-helically symmetric magnetic configuration. The helical coordinate system best describes the path of the wave launched from each antenna as well as the position of each ECRH antenna. In this coordinate system, the helical cut of the plasma is defined perpendicular to the magnetic-axis, which at the ECRH antenna position is pitched 28.8° with respect to the vertical direction. An isometric view of the vacuum vessel representation used in multi-pass ray tracing calculations in section 4 is shown in figure 1, with a half-field period removed to reveal the LCFS. The TRAVIS code requires that the vacuum vessel model be continuous; consequently, the vacuum vessel model does not include ports, and it is not an exact replica of the HSX vacuum vessel.

The first ECRH antenna launches the wave perpendicular to the magnetic flux surfaces along the plasma midplane toward the magnetic axis from the low field side of the device. The second ECRH antenna is positioned 9 cm below the plasma midplane within the helical cut that is perpendicular to the magnetic axis. The wave intensity of each beam is modeled as a Gaussian profile, which is specified by its beam waist and focal length in the TRAVIS code [6]. The half-widths of each beam at the LCFS are 32 and 34 mm for the first and second antenna respectively (defined at the e^{-2} power level). The beam incident on the plasma from each antenna is divergent and the angular divergence is estimated to be 20 degrees. A beam radius of 16.7 cm and a focus 19.1 cm behind each antenna was used in the code to reproduce these parameters. The wave launched by each antenna is discretized into 33 annuli, with 45 rays per ring, which are concentric about a central ray representing the beam-axis. The annuli are equally distributed radially, and the rays are distributed equally about each ring in the azimuthal direction. This ray distribution was obtained by iterating the number of rays until the absorbed power profile and the total absorbed power converged. The cold plasma dispersion relation is used to calculate ray trajectories in HSX, and the anti-Hermitian portion of the fully relativistic dielectric tensor is used to calculate the absorption [5].

3. Single-pass absorption calculations and initial ECRH results

The second ECRH antenna is capable of depositing ECRH power from 10 cm above the magnetic axis to 18 cm below. The ray trajectories launched at $\theta = 10°$ with respect to the major radius from the second antenna are shown in figure 2. The absorption profiles calculated for three magnetic field strengths at this launch angle are shown in figure 3. As the resonance moves off-axis, wave refraction can become significant in the presence of a density gradient, and ray tracing calculations are necessary to determine the resonance location in the plasma.

The plasma density and magnetic field gradients are parallel to the central ray launched from the first antenna, and the gradients are symmetric, relative to the axis of the beam. The central ray of the first beam does not refract, while the beam
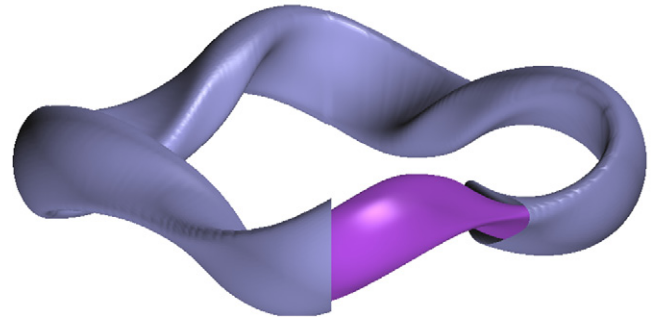

Figure 1. The vacuum vessel representation used in multi-pass ray tracing calculations (blue) with a half-field period removed to reveal the LCFS (purple).
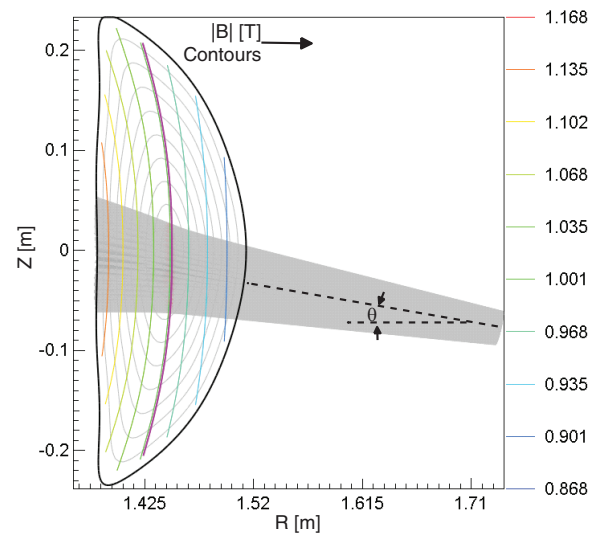

Figure 2. A projection of the rays launched from the second antenna into the vertical plane of the launcher.
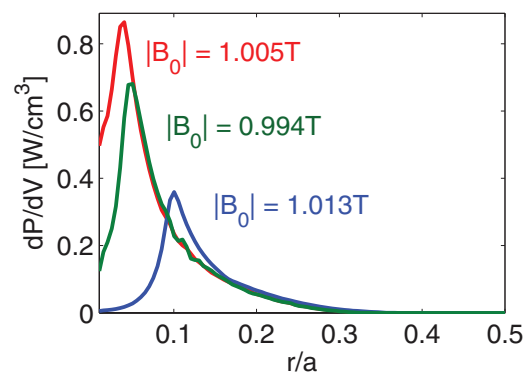

Figure 3. Absorption profiles and absorbed power for three magnetic field strengths at a $\theta = 10°$ launch angle, and a launched power of 50 kW.

width is increased due to refraction. At a mirror launching angle of $\theta = 15°$ with respect to the major radial direction, the wave from the second antenna is launched towards the magnetic axis. The plasma density and magnetic field gradients are oblique to the axis of the beam launched by the second
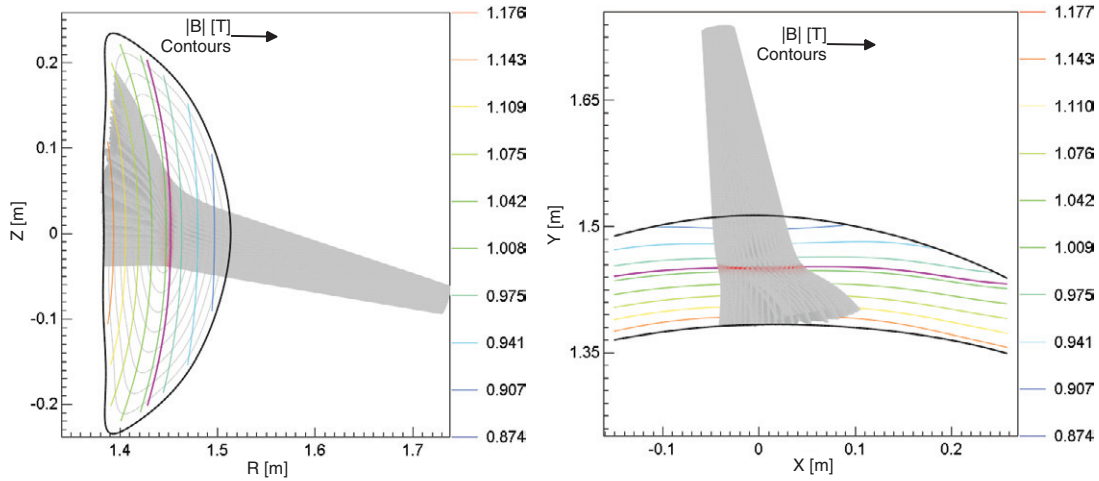
Figure 4. Two projections of rays launched from the second antenna. A vertical plane (left) and a horizontal plane (right) are shown.

antenna, and its central ray refracts, especially at moderate to relatively higher plasma densities. Figure 4 shows two projections of the ray trajectories launched toward the magnetic axis from the second ECRH antenna at an angle of $\theta = 15°$ in a plasma with a central density of $8 \times 10^{18}\,\mathrm{m}^{-3}$

A launch angle scan with 1 T on-axis magnetic field was performed in plasma produced and maintained solely by 50 kW of ECRH power from the second antenna. Peaked stored energies and electron temperatures were measured while aiming the beam slightly below the magnetic axis. Thomson scattering measurements of the plasma electron density and temperature are shown in figure 5. The single-pass absorption calculation does not predict on-axis heating for the 5° launch angle case, and multi-pass calculations are necessary to reproduce the experimentally observed dependence on launching angle. These calculations are discussed in section 4. The axis of the second beam is refracted away from the core of HSX at plasma density shown in figure 5, resulting in low absorption. The absorbed power density drops quickly outside of the core for these cases, and low electron temperatures and high electron density gradients are commonly measured in plasmas produced solely by ECRH power launched from the second antenna.

The electron temperature and density profiles for a plasma supported by both ECRH systems are shown in figure 6. When 50 kW of ECRH power is launched from the second antenna at a launch angle of 15° into a target plasma supported by 50 kW of ECRH power from the first antenna, the stored energy, electron temperature and density profiles are comparable to those of plasma supported by 100 kW of ECRH power solely from the first antenna. The calculated absorption is higher and the absorbed power profile is more peaked with a target plasma where higher stored energies and electron temperatures are observed.

The magnetic field strength, central plasma density, and central electron temperature were scanned and the corresponding first-pass absorption and its profile calculated by TRAVIS are shown in figure 7. The experimental data set from figure 6 is also shown in figure 7 for comparison.
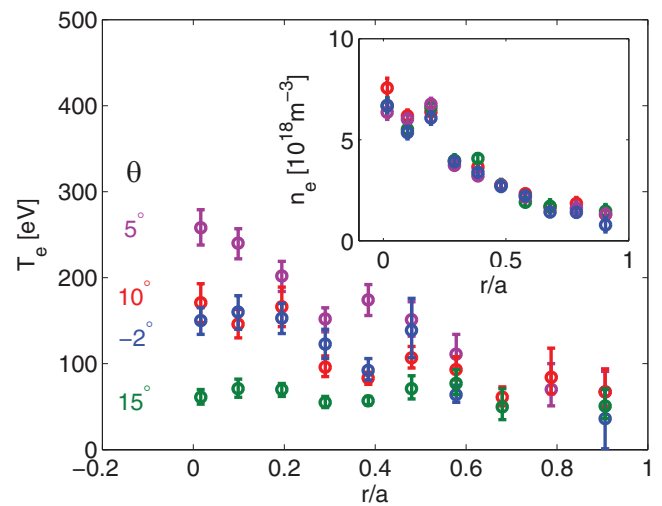

Figure 5. Electron temperature and plasma density profile at four launching angles for a plasma produced and maintained by 50 kW of ECRH power launched solely from the second antenna.

Row (*a*) of figure 7 shows the effect of varying the central magnetic field on the ray tracing calculations. Similarly, the effect of varying the central plasma density and central electron temperature on the calculations are shown in row (*b*) and row (*c*) respectively. Column 1 of figure 7 shows the plasma density, electron temperature, and magnetic field strength used for the ray tracing calculations. Column 2 shows the single-pass absorption efficiency for power launched from each antenna independently, and column 3 shows the total calculated absorbed power normalized to the launched power.

The absorption efficiency of power launched from the first antenna (ECRH1) is slightly lower than the absorption efficiency of power launched from the second antenna (ECRH2) for most of the cases in figure 7, because the wave launched from ECRH2 has a longer path through the plasma than the wave launched from ECRH1.

In row (*a*) of figure 7, the absorption efficiency increases as the cold plasma resonance moves from the high field side
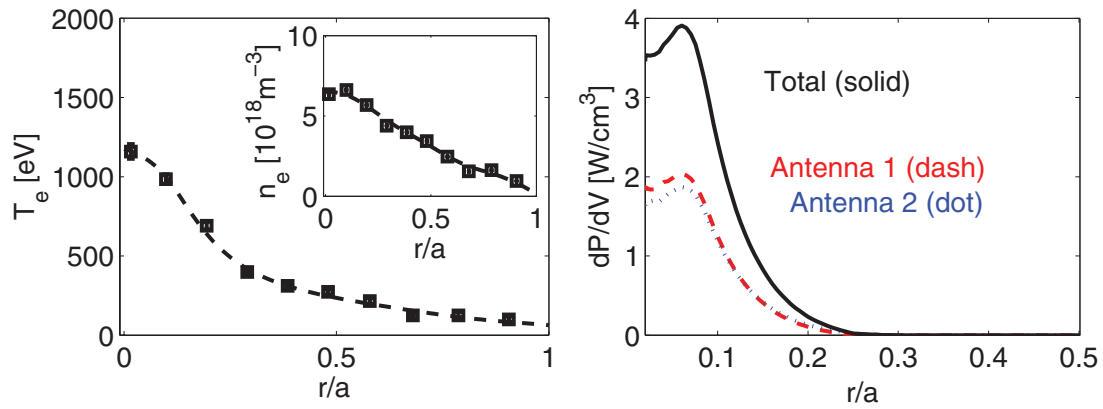
Figure 6. Electron temperature (left) and density (inset, left) and calculated power deposition profile for 1.01 T on-axis magnetic field (right) using both ECRH systems.
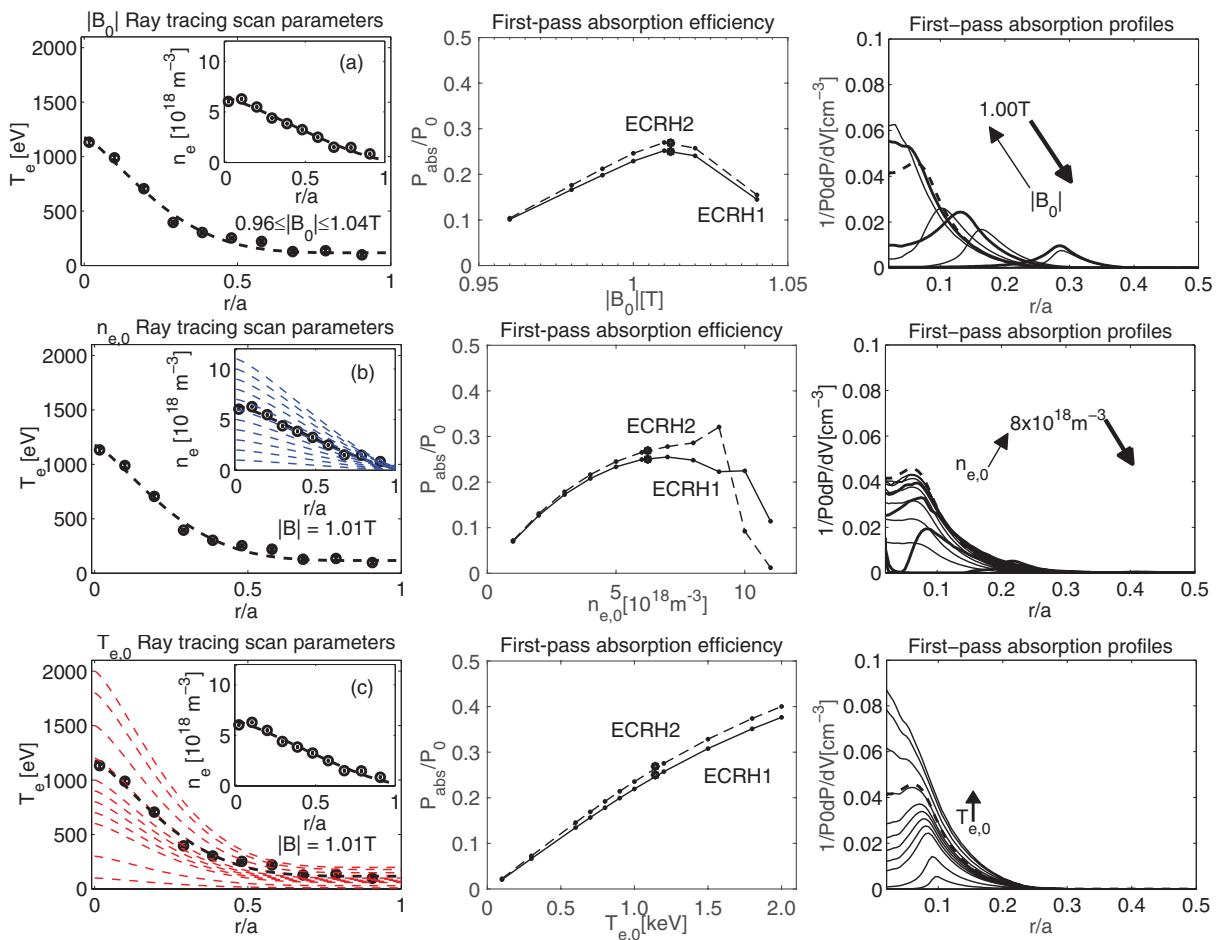

Figure 7. Simulated n_e and T_e profiles (column 1), and predicted single-pass absorption (column 2) and its profile (column 3) as a function of main magnetic field (row (*a*)), plasma density (row (*b*)) and electron temperature (row (*c*)). The experimental result from figure 6 is also shown (dashed line in column 1 + 3, asterisk in column 2).

to a location slightly on the low-field side of the magnetic axis. Above 1.01 T, the absorption efficiency decreases as the cold plasma resonance moves further away from the magnetic axis. The relativistic downshift of the resonance frequency causes the absorption profile to remain peaked as the

on-axis magnetic field increases from 1.00 T to 1.01 T, and the same effect causes asymmetry between the high-field side heating cases (0.96–1.00 T), and the low-field side heating cases (1.01–1.04 T). In row (*b*), the first-pass absorption efficiency increases with plasma density, as expected for 1st

harmonic ordinary mode ECRH [9], until it approaches the cut-off value. Wave refraction strongly modifies the absorption profile, which becomes hollow and eventually decreases in magnitude above a central plasma density of approximately $8 \times 10^{18}\,\mathrm{m}^{-3}$.

Similarly in row (*c*), the electron temperature is the only parameter that changes and both the absorption efficiency for each antenna and the peak in the absorption profile increase approximately linearly with the temperature at the resonance. The relativistic effect causes the absorption to peak with increasing electron temperature, because the cold plasma resonance is located at approximately 10% of the minor radius on the low-field side of the magnetic axis.

4. Multi-pass ray tracing calculations and comparison to measurements

The operating density of HSX leads to low absorption of the launched power during the first-pass through the plasma. After its first pass through the plasma, the beam is reflected from the stainless steel vessel wall and undergoes multiple reflections before it is absorbed by the plasma. Electron cyclotron waves are strongly damped in the toroidal direction in HSX and an effective reflection coefficient of 0.9 was inferred from absorption measurements [10].

The experimental absorbed power is determined using the difference in energy balance before and after ECRH turn-off, $P_{\mathrm{abs}} = \frac{\mathrm{d}W_{\mathrm{E}}}{\mathrm{d}t}\big|_{t^+}^{t^-}$, by measuring the change in electron temperature and density using a 10-channel Thomson scattering diagnostic and then integrating the profiles. The experimental absorption efficiency is measured to be 45%, which is higher than the 30% first-pass absorption calculated from ray tracing. The decay of the energy in the integrated profiles is shown in figure 8, along with the linear fits that are used to determine the temporal derivative of the stored energy.

The total absorbed power is measured to be $39 \pm 4\,\mathrm{kW}$. The characteristic decay rate of the plasma stored energy is representative of the energy confinement time which is inferred from energy balance to be $\tau_{\mathrm{E}} = W_{\mathrm{E}}/P_{\mathrm{abs}} = 1.5 \pm 0.1$ ms in HSX.

Reflection from the HSX vacuum vessel is modeled using the TRAVIS code and higher multi-pass absorption is calculated for ECRH1 than for ECRH2. Figure 9 shows the projection of the ray trajectories into the vertical plane after their first reflection from the vacuum vessel wall for the beam launched from the first antenna. The central chord of the beam is reflected back through the plasma core. Although the beam divergence of the second pass through the plasma is larger than the beam divergence of the first pass, the majority of the absorption occurs in the hot, dense core of HSX resulting in high localization of the absorption. The beam divergence is large, and the absorbed power density is small after the first pass through the plasma leading to lower multi-pass absorption outside of the core of the plasma.

Figure 10 shows the projection of the ray trajectories from the second antenna into the vertical plane after their first reflection from the vacuum vessel wall. In addition to a
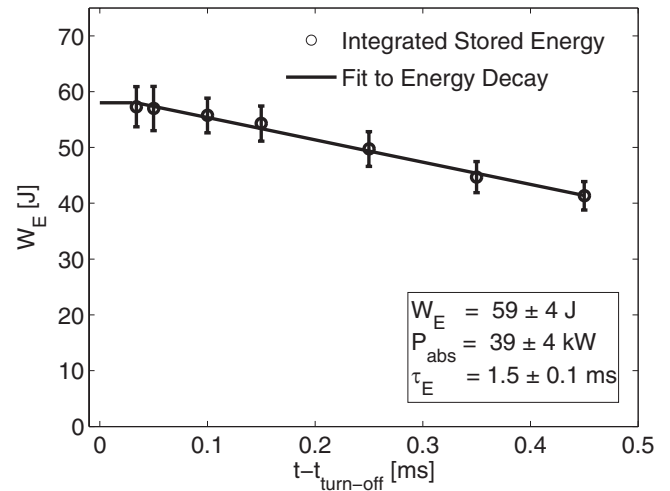

Figure 8. The absorbed power, P_{abs}, is measured from the decay rate of the integrated plasma stored energy, W_{E} (circles), using Thomson scattering (black) measurements after ECRH turn-off.

large beam divergence and resulting low density of absorbed power, the beam-axis travels away from the hot, dense plasma core. These effects result in the majority of the absorption coming from the first pass through the plasma. There is very little absorption outside of the plasma core and the deposition profile of ECRH power launched from the second antenna remains localized within $r/a \leqslant 0.2$. The multi-pass absorption calculations shown in figures 9 and 10 are summarized in table 1.

The present version of the TRAVIS code does not take into account wave polarization changes upon wall reflection or wave refraction by density gradients outside of the last closed magnetic surface. Additionally, the code is not capable of modeling ports in the vacuum vessel. These effects result in lower absorbed power density and smaller multi-pass absorption [6]; however, previous measurements have shown that the toroidal damping length in HSX is short [10]. The absorption profiles shown for ECRH1 in figure 9, and for ECRH2 in figure 10, should be interpreted as upper limits for the absorption after three passes through the plasma in HSX.

The single- and multi-pass absorption profile calculations for the mirror angle scan presented in figure 5 are shown in figure 11. The peak electron temperature in figure 5 is achieved with a launch angle of 5°, but the single-pass absorption calculation that is shown at left in figure 11, predicts core heating at a launch angle of 10°. Modeling of the multi-pass absorption has been used to investigate its effect on the electron temperature profile peaking. The multi-pass calculations shown at right in figure 11 predict on-axis heating for the 5° launch angle case and partially support the measured electron temperature profile in the 10° case, but not the −2° case, where a similar electron temperature profile is measured. The multi-pass absorption is sensitive to the geometry of the vacuum vessel, and a more precise vacuum vessel model may be necessary to reproduce this behavior. Another factor that can affect the power density is wave propagation through the scrape-off-layer region.
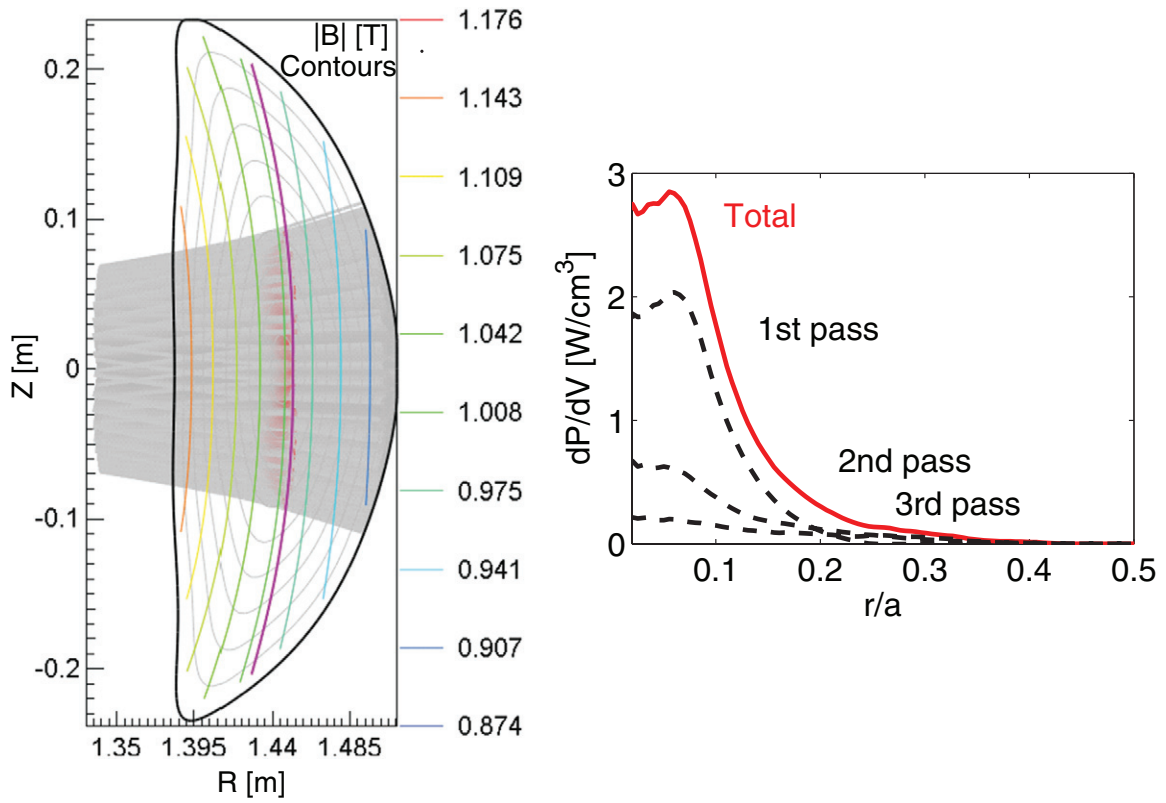
Figure 9. A projection of the rays launched from ECRH1 into the vertical plane during their second pass through the plasma (left) and the absorption profiles calculated for each pass (right).
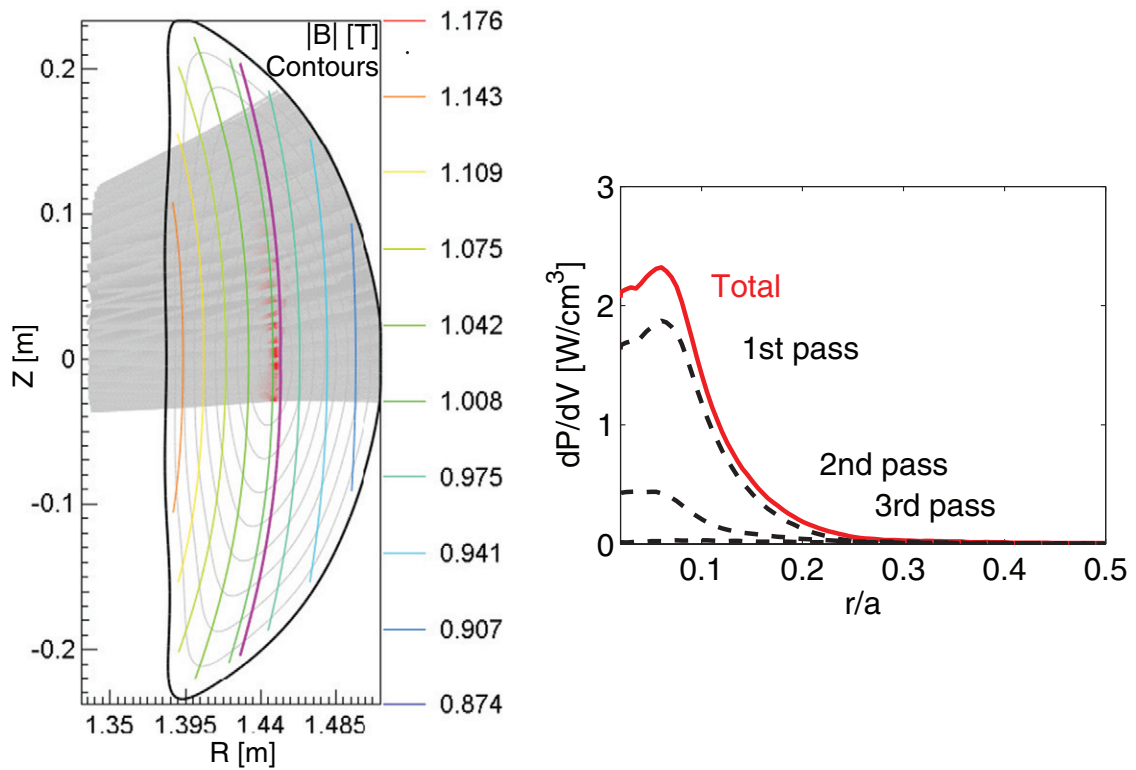
Figure 10. A projection of the rays launched from ECRH2 into the vertical plane during their second pass through the plasma (left) and the absorption profiles calculated for each pass (right).

Table 1. Launched and absorbed power from multi-pass ray tracing calculations for ECRH1 and ECRH2.

	P_{launched} (kW)	P_{abs} total (kW)	1st pass (kW)	2nd pass (kW)	3rd pass (kW)
ECRH1	50	20	11	6	3
ECRH2	50	15	11	3	1
Combined	100	35	22	9	4
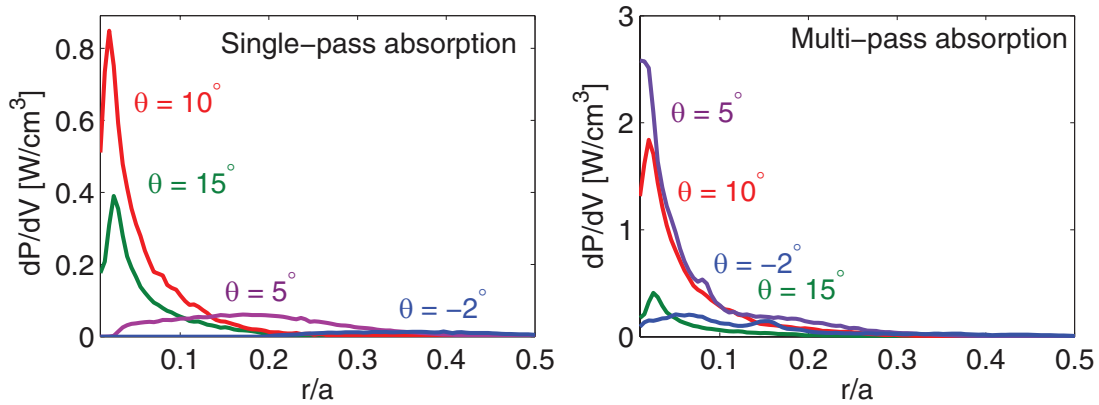
Figure 11. Single-pass (left) and multi-pass (right) absorption profiles calculated at four launching angles for a plasma produced and maintained by 50 kW of ECRH power launched solely from the second antenna.

5. Conclusions

A second gyrotron with a hybrid transmission line has been installed and tested on HSX. The second antenna includes a steerable mirror for off-axis heating, and the output power of the second gyrotron can be modulated to facilitate heat pulse propagation experiments [11]. Ray tracing calculations are used to model the absorption of ECRH launched from both antennas. Refraction modifies the propagation and absorption of the beam launched from the second antenna with the beam-axis deviating strongly from straight propagation. The TRAVIS code predicts 30% single-pass absorption efficiency of the ordinary wave at the fundamental resonance frequency in HSX, while the subsequent passes through the plasma increase the total efficiency up to the measured absorption efficiency of 45%. It has been shown that the heating from the first launcher is reinforced by multi-pass absorption, while the heating from the second antenna is less sensitive.

Acknowledgments

References

[1] ITER Physics Expert Group on Energetic Particles 1999 Heating and current drive and ITER Physics Basis Editors *Nucl. Fusion* **39** 2495
[2] Anderson F.S.B., Almagri A.F., Anderson D.T., Matthews P.G. and Talmadge J.N. 1995 *Fusion Technol.* **27** 273
[3] Almagri A.F., Anderson D.T., Anderson F.S.B., Probert P.H., Shohet J.L. and Talmadge J.N. 1999 *IEEE Trans. Plasma Sci.* **27** 114
[4] Anderson D.T., Almagri A.F., Anderson F.S.B., Gerhardt S.P., Radder J. and Talmadge J.N. 2002 *J. Plasma Fusion Res.* **78** 209
[5] Marushchenko N.B., Erckmann V., Hartfuss H.J., Hirsch M., Laqua H.P., Maassberg H. and Turkin Y. 2007 *J. Plasma Fusion Res.* **2** S1129
[6] Marushchenko N.B., Turkin Y. and Maassberg H. 2014 *Comput. Phys. Commun.* **185** 165
[7] Boozer A.H. 1983 *Phys. Fluids* **26** 496
[8] Hirshman S.P. and Whitson J.C. 1983 *Phys. Fluids* **26** 3553
[9] Alikaev V.V., Suvorov E.V. and Friman A.A 1992 *High-Frequency Plasma Heating* ed A. G Litvak (New York: AIP) p 3
[10] Likin K.M. *et al* 2003 *Plasma Phys. Control. Fusion* **45** A133
[11] Weir G.M., Faber B.J., Likin K.M., Talmadge J.N., Anderson D.T. and Anderson F.S.B. 2015 *Phys. Plasmas* **22** 056107